Density Functional Study of Electron Paramagnetic Resonance Parameters and Spin Density Distributions of Dicopper(I) Complexes with Bridging Azo and Tetrazine Radical-Anion Ligands

Christian Remenyi, Roman Reviakine, and Martin Kaupp*

Institut für Anorganische Chemie, Universität Würzburg, Am Hubland, D-97074 Würzburg, Germany

Received: December 31, 2005; In Final Form: February 1, 2006

There exists a growing class of dinuclear complexes with bridging radical-anion ligands that is of interest both for bioinorganic and for supermolecular chemistry. Their bonding situation as well as chemical and spectroscopic properties are not described adequately by standard models such as the ligand-field theory. For rational design of complexes with desired properties, it is thus necessary to understand better the interrelations between electronic structure, spin density, and electron paramagnetic resonance (EPR) parameters in dinuclear systems with redox-active bridging ligands and to evaluate the performance of density functional methods in their description. As particularly suitable, experimentally well-characterized representatives, a series of dinuclear copper(I) complexes with azo or tetrazine bridge ligands have been studied here by different density functional methods. To reproduce the available experimental metal hyperfine couplings, the inclusion of spin−orbit effects into the calculations is necessary. An unusual direction of the dependence of computed hyperfine couplings on an exact-exchange admixture into the exchange-correlation functional may be understood from a McConnell-type spin polarization of the σ-framework of the bridge. Ligand nitrogen hyperfine couplings are also compared with experiment where available. Electronic **g**-tensors are reproduced well by the calculations and have been analyzed in detail in terms of atomic spin−orbit contributions and electronic excitations.

1. Introduction

Transition-metal complexes with redox-active radical-anion ligands have been investigated intensively during the past decade. This interest is fuelled on one side by their role as models for certain metalloenzymes such as galactose oxidase or related systems[1] and on the other side by their potential as building blocks in supermolecular architectures with interesting electron-transfer and magnetic properties.[2] In the case of a radical anion bridging two metals, a main challenge is to establish reasonable physical oxidation states for metals and ligand together with a reliable spin density distribution. Often, electron paramagnetic resonance (EPR) spectroscopy is used in this context.[3] The delocalized nature of the spin density renders such paramagnetic systems with "noninnocent" bridging ligands, which are interesting from both spectroscopic and theoretical points of view. In particular, the standard ligand-field models, that are often applied to interpret the EPR data (hyperfine couplings and **g**-tensors) of "normal" transition-metal complexes with metal-centered spin,[4] are not applicable to these more unusual bonding situations. At the same time, simple models that are common for interpreting the EPR parameters of organic π-radicals[5,6] also need to be extended when the spin is appreciably delocalized onto transition-metal centers. The recent, tremendous development of quantum chemical methods for the computation of magnetic-resonance parameters[7] provides many of the necessary more quantitative tools to be applied in these cases, and detailed benchmark studies are required to translate these sometimes sophisticated calculations into useful, qualitative models for bonding and spin density distribution.

Our recent work on systems with redox-active ligands has focused on a series of dirhenium complexes with bridging azo ligands,[8] where we have tried to analyze by DFT calculations data obtained by high-field EPR (and on Ru complexes with *ortho*-quinonoid ligands[9]). Due to the importance of higher-order spin−orbit effects and a large dependence of the results on exchange-correlation functional, the computation of electronic **g**-tensors for such systems turned out to be particularly challenging. Hyperfine data were not available for comparison. To establish the accuracy of DFT methods for both hyperfine and **g**-tensors of such radical-anion dinuclear complexes in a more meaningful and complete way, and to provide a basis for qualitative models, we extend our quantum chemical analyses now to a series of monocationic dicopper complexes $[(\mu\text{-}L_b)(CuL_2)_2]^{\bullet+}$. The dichelating tetradentate ligand L_b contains an azo or tetrazine moiety (Scheme 1), and the spin density is thought to be concentrated mostly on L_b. These interesting systems (with PPh_3 or $Ph_2P(CH_2)_6PPh_2$ coligands L) have recently been studied in detail experimentally by Kaim and coworkers.[10−13] The advantages of this choice of target systems for deeper theoretical study are 3-fold: (a) For the 3d metal copper, the **g**-tensor is expected to be described better by a perturbational treatment of spin−orbit coupling than for the above-mentioned dirhenium systems. This should allow a better assessment of the performance of different density functionals and a more transparent interpretation of the **g**-tensors in terms of electronic structure. (b) Both metal and ligand hyperfine data are available for the title systems.[10,11,13,14] These provide an additional testing ground for evaluating the performance of different exchange-correlation potentials for the description of the spin density distribution and also a check of the importance of spin−orbit corrections to hyperfine couplings. (c) Copper

* To whom correspondence should be addressed. E-mail: kaupp@mail.uni-wuerzburg.de.

10.1021/jp057594i CCC: $33.50
Published on Web 02/28/2006

SCHEME 1 Formulas of the Investigated Complexes[a]

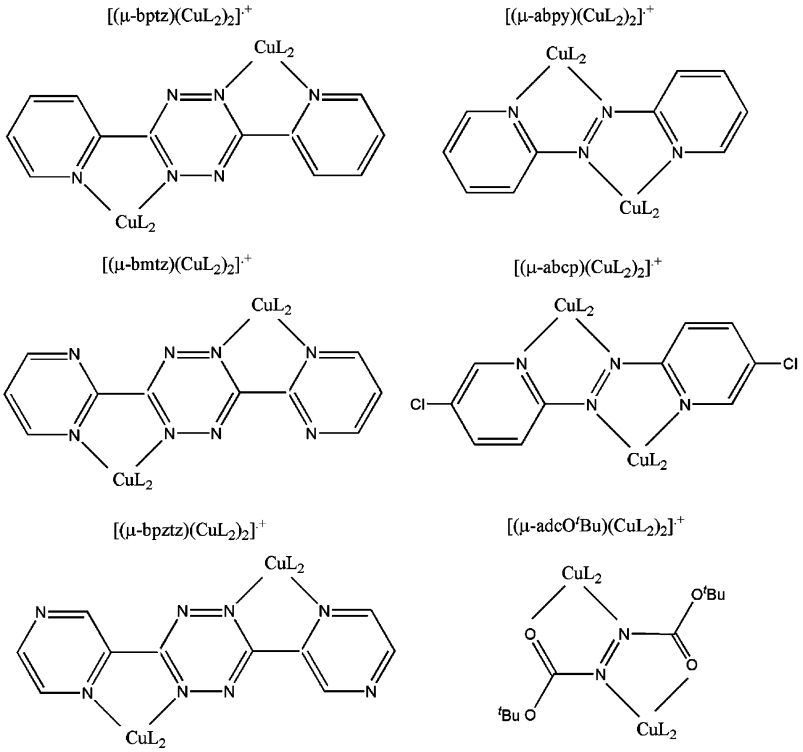

[a] Unless noted otherwise, the coligands L have been chosen to be phospine PH_3 ligands in the calculations. Experimentally studied examples had either PPh_3 ($[(\mu\text{-bptz})(CuL_2)_2]^{\bullet+}$, $[(\mu\text{-bmtz})(CuL_2)_2]^{\bullet+}$, $[(\mu\text{-abcp})(CuL_2)_2]^{\bullet+}$) or $Ph_2P(CH_2)_6PPh_2$ coligands ($[(\mu\text{-abpy})(CuL_2)_2]^{\bullet+}$, $[(\mu\text{-adcO}^t\text{Bu})(CuL_2)_2]^{\bullet+}$).

complexes with radical-anion ligands are of particular interest in the context of galactose oxidase or related radical metalloenzymes.[1] The aim of this study is to provide a detailed understanding of the interrelations between EPR parameters and spin density distributions of such nonstandard delocalized dinuclear complexes.

2. Theoretical Formalism

The theoretical background of EPR parameters is covered in detail in various text books.[15−20] Here, we will summarize only the most relevant points.

Hyperfine Tensor Calculations. In the usual nonrelativistic first-order approximation, isotropic hyperfine splittings $A_{iso}(N)$ correspond to the Fermi-contact term A^{FC}

$$A_{iso}(N) = A^{FC} = \frac{4\pi}{3}\beta_e\beta_N g_e g_N \langle S_z\rangle^{-1} \sum_{\mu,\nu} P^{\alpha-\beta}_{\mu,\nu}\langle\phi_\mu|\delta(\mathbf{R}_N)|\phi_\nu\rangle \quad (1)$$

Here, β_e is the Bohr magneton, β_N the nuclear magneton, g_N is the g-value of nucleus N, $\langle S_z\rangle$ is the expectation value of the z-component of the total electronic spin, $P^{\alpha-\beta}_{\mu,\nu}$ is the spin density matrix, and the summation runs over all occupied molecular orbitals. The components $\mathbf{A}^{dip}_{ij}(N)$ of the anisotropic tensor are given by

$$\mathbf{A}^{dip}_{ij}(N) = \frac{1}{2}\beta_e\beta_N g_e g_N \langle S_z\rangle^{-1} \sum_{\mu,\nu} P^{\alpha-\beta}_{\mu,\nu}\langle\phi_\mu|\mathbf{r}_N{}^{-5}(\mathbf{r}_N{}^2\delta_{ij} - 3\mathbf{r}_{N,i}\mathbf{r}_{N,j})|\phi_\nu\rangle \quad (2)$$

where $r_N = r - R_N$ (R_N is the position vector of nucleus N). In the rest of this section, we will refer to the metal hyperfine interaction and omit the subscript N. Spin−orbit (SO) corrections to **A** have been shown to give nonnegligible contributions to the total **A**-tensor already in the 3d series.[21,22] In the present study, SO corrections to **A** were obtained from second-order perturbation theory. At the coupled-perturbed Kohn−Sham level, the dominant SO correction term arises as a second-order cross term between the one- and two-electron SO Hamiltonian h^{SO} and the perturbed Fock operator F'_K

$$\mathbf{A}^{SO-I}_{K,uv} = \frac{1}{2}\alpha^4 g_e \gamma_K \frac{1}{2\langle S_z\rangle} \times \left[\sum_k^{occ(\alpha)}\sum_a^{virt(\alpha)} \frac{\langle\psi^\alpha_k|h^{SO}_u|\psi^\alpha_a\rangle\langle\psi^\alpha_a|F'_{K,v}|\psi^\alpha_k\rangle}{\epsilon^\alpha_k - \epsilon^\alpha_a} - \sum_k^{occ(\beta)}\sum_a^{virt(\beta)} \frac{\langle\psi^\beta_k|h^{SO}_u|\psi^\beta_a\rangle\langle\psi^\beta_a|F'_{K,v}|\psi^\beta_k\rangle}{\epsilon^\beta_k - \epsilon^\beta_a}\right] \quad (3)$$

where α is the fine-structure constant, γ the gyromagnetic ratio of the nucleus, h_{SO} is explained below, and F'_K is the perturbed Fock operator, with $F'_K = (l_v/r^3) - (2/\alpha)a_0 \sum_{k=1}^{n/2} K'_{k,v}$ where (l_v/r^3) is the paramagnetic nuclear-spin electron-orbit (PSO) operator, $K'_{k,v}$ is the response exchange operator, and a_0 is the weight of HF exchange depending on the specific hybrid functional used (detailed descriptions of our implementation[23,24] are provided in refs 23 and 24; see ref 21 for a related simultaneous CPKS implementation and both works for references to earlier implementations). ψ^σ and ϵ^σ are spin-polarized Kohn−Sham orbitals and orbital energies, respectively. GGA or LDA functionals lead to an uncoupled DFT (UDFT) treatment for this second-order term ($a_0 = 0$). For better comparison with experimental values, the SO correction to **A** (*ii* denotes principal components) is given in terms of an isotropic pseudocontact (A^{PC}) and traceless dipolar ($\mathbf{A}^{"dip,2"}$) term

$$\mathbf{A}^{total}_{K,ii} = A^{PC}_K + \mathbf{A}^{dip,2}_{K,ii} \quad (4)$$

g-Tensor Calculations. The **g**-tensor will be provided as the correction to the free-electron value (given in ppt, i.e., in units of 10^{-3})

$$\mathbf{g} = g_e 1 + \Delta\mathbf{g} \tag{5}$$

with $g_e = 2.002319$. Up to the level of second-order perturbation theory based on the Breit−Pauli Hamiltonian, the *g*-shift $\Delta\mathbf{g}$ consists of three terms

$$\Delta\mathbf{g} = \Delta\mathbf{g}^{\mathrm{SO/OZ}} + \Delta\mathbf{g}^{\mathrm{RMC}} + \Delta\mathbf{g}^{\mathrm{GC}} \tag{6}$$

of which the "paramagnetic" second-order spin−orbit/orbital Zeeman cross term, $\Delta\mathbf{g}^{\mathrm{SO/OZ}}$, dominates (except for extremely small Δg values).[15] Within the coupled-perturbed Kohn−Sham (CPKS) scheme, using (nonlocally implemented) hybrid density functionals, and based on unrestricted Kohn−Sham calculations, the Cartesian components $\Delta\mathbf{g}_{uv}$ are computed as

$$\Delta g_{uv}^{\mathrm{SO/OZ}} = \frac{\alpha^2}{2} g_e \left[\sum_k^{\mathrm{occ}(\alpha)} \sum_a^{\mathrm{virt}(\alpha)} \frac{\langle \psi_k^\alpha | h_v^{\mathrm{SO}} | \psi_a^\alpha \rangle \langle \psi_a^\alpha | F'_{k,u} | \psi_k^\alpha \rangle}{\epsilon_k^\alpha - \epsilon_a^\alpha} - \sum_k^{\mathrm{occ}(\beta)} \sum_a^{\mathrm{virt}(\beta)} \frac{\langle \psi_k^\beta | h_v^{SO} | \psi_a^\beta \rangle \langle \psi_a^\beta | F'_{k,u} | \psi_k^\beta \rangle}{\epsilon_k^\beta - \epsilon_a^\beta} \right] \tag{7}$$

with $F'_K = l_O - (2/\alpha)a_0 \sum_{k=1}^{n/2} K'_{k,v}$. l_O is a spatial component of the orbital Zeeman operator. The relativistic mass correction term $\Delta\mathbf{g}^{\mathrm{RMC}}$ and the one-electron part of the gauge correction term $\Delta\mathbf{g}^{\mathrm{GC}}$ are also included in our implementation[25,26] (see also refs 27 and 28 for related implementations).

3. Computational Details

Unless noted otherwise, the substituents at the phosphine coligands have been replaced by hydrogen atoms (see Scheme 1). In a number of cases, calculations with L = PPh_3 have been added. All structures were optimized without symmetry restrictions at the BP86 DFT level,[29,30] using unrestricted Kohn−Sham wave functions and the Turbomole 5.6 program.[31] The Coulombic term was approximated by density fitting ("RI-DFT" method).[32] Orbital basis sets and auxiliary basis sets for density fitting were of SVP quality.[33]

For the EPR property calculations, unrestricted DFT single-point calculations of the wave functions at the optimized structures were performed with Turbomole using a (15s11p6d)/[9s7p4d] Cu basis set designed for hyperfine calculations[32] and employed also in our previous studies of 3d complexes.[34,35] Ligand atoms were treated by Huzinaga−Kutzelnigg-type basis sets BII (sometimes also denoted as IGLO-II).[36,37] The following exchange-correlation functionals were compared: (a) the BP86 GGA functional[29,30] (without density fitting), (b) the hybrid B3LYP functional[38,39] with 20% exact exchange, and (c) the hybrid BHLYP functional with 50% exact exchange.[40,41] The unrestricted Kohn−Sham orbitals were transferred to the MAG-ReSpect property package[42] by suitable interface routines.[25,26] The atomic mean-field approximation (AMFI)[43,44] has been used to compute the matrix elements of the spin−orbit (SO) operator, h^{SO}, in eqs 3 and 7. In **g**-tensor calculations, we employed a common gauge at the center of mass. While no symmetry restrictions were introduced into the calculations, the hyperfine coupling (HFC) tensors for all ligand atoms in approximately diagonal positions are very similar (differences < 0.5 MHz), and average values are provided in the Tables. All HFC tensor results are reported in MHz.

To break down the FC term into the contributions from individual molecular orbitals, we recall that the spin density matrix is $P_{\mu\nu}^{\alpha-\beta} = \sum_K^{N\alpha} C_{\mu K}^\alpha C_{\nu K}^\alpha - \sum_K^{N\beta} C_{\mu K}^\beta C_{\nu K}^\beta$, where $C_{\mu K}^\gamma$, $\gamma = \overline{\alpha,\beta}$ are the MO coefficients and the sum runs over all occupied MOs. One may then rewrite eq 1 in terms of molecular orbitals ψ_K

$$A_{\mathrm{iso},N} = \frac{4\pi}{3} \beta_e \beta_N g_e g_N \langle S_z \rangle^{-1} \left(\sum_K^{N\beta} (h_{\mathrm{FC}}^{\alpha,K} - h_{\mathrm{FC}}^{\beta,K}) + \sum_{K>N\beta}^{N\alpha} h_{\mathrm{FC}}^{\alpha,K} \right)$$

$$h_{\mathrm{FC}}^{\gamma,K} = \langle y_K^\gamma(r_{Ni}) | \delta(r_{Ni}) | \psi_K^\gamma(r_{Ni}) \rangle, \gamma = \overline{\alpha,\beta} \tag{8}$$

The first sum in parentheses in eq 8 corresponds to the contributions from the doubly occupied MOs while the last sum corresponds to the contributions from the singly occupied MOs. In the case of strong spin polarization, the energy ordering within the α- and *β*-subsets may differ. We have ensured matching of the corresponding spatial parts of $\psi_L{}^\alpha$, $\psi_K{}^\beta$ by a maximum overlap criterion

$$\langle \psi_K{}^\beta | \psi_L{}^\alpha \rangle \overset{!}{=} \max, \quad L = (1..N_\alpha) \tag{9}$$

Natural population analyses (NPAs),[45] which were used to analyze spin populations, have been carried out with a standalone version of the NBO4.M program,[46] which has been interfaced to Turbomole by an in-house routine.[47] Isosurface plots of spin density distributions and molecular orbitals were performed with Molekel.[48]

4. Results and Discussion

Structures. Table 1 compares selected structural parameters of four representatives of the investigated complexes, $[(\mu\text{-bptz})(Cu(PH_3)_2)_2]^{\bullet+}$, $[(\mu\text{-bptz})(Cu(PPh_3)_2)_2]^{\bullet+}$, $[(\mu\text{-abcp})(Cu(PH_3)_2)_2]^{\bullet+}$, and $[(\mu\text{-abcp})(Cu(PPh_3)_2)_2]^{\bullet+}$, with experimental crystallographic structures, which are available[13,49] for the corresponding $[(\mu\text{-bptz})[Cu(PPh_3)_2]_2](BF_4)$ and $[(\mu\text{-abcp})[Cu(PPh_3)_2]_2](PF_6)$ complexes. The computed bond lengths differ from the experimental ones by maximally 0.05 Å. The largest deviations occur for the Cu−N bonds, whereas bond lengths within the bridging ligand agree almost perfectly with experiment. The calculated N3CuN1 angles (for numbering, see Scheme 2) are also reproduced well. Comparing the calculated structures of the complexes with L = PH_3 and L = PPh_3, we found that the bulky triphenylphosphine ligands lead to a twisting between the tetrazine and pyridine ring systems. However, the structure of the tetrazine ring itself and the Cu−N bonds and angles are not affected much. Some of the parameters computed for the smaller bptz-model and abcp-model systems do actually agree better with experiment than those calculated for the "real" systems. This appears to be a compensation between systematic DFT errors (at the BP86 level one expects somewhat too long metal−ligand distances) and the electronic influence of the phenyl substituents. Assuming a similar compensation also for the other models with PH_3 coligands, we expect that the computed model structures should be very appropriate to analyze the electronic structure and EPR parameters of the investigated complexes. Cartesian coordinates of all complexes studied here are given in the Supporting Information.

Spin Density Distribution. Of the six monocationic $[(\mu\text{-}L_b)(Cu(PH_3)_2)_2]^{\bullet+}$ complexes studied here, three exhibit a tetrazine moiety and three an azo system as bridging tetradentate ligand

TABLE 1: Comparison of Experimental Structures[a] with Calculated Ones (RI-BP86)

	Cu−N1	Cu−N3	Cu−P[b]	N1−N2	N1−C1	N3−C2	<N3CuN1
$[(\mu\text{-bptz})(Cu(PH_3)_2)_2]^{\bullet+}$ calcd	2.020	2.088	2.264	1.370	1.374	1.361	81.5
$[(\mu\text{-bptz})(Cu(PPh_3)_2)_2]^{\bullet+}$ calcd	2.050	2.132	2.304	1.378	1.365	1.361	79.4
$[(\mu\text{-bptz})(Cu(PPh_3)_2)_2]^{\bullet+}$ exp[49]	2.032	2.084	2.287	1.394	1.338	1.355	79.5
	Cu−N1	Cu−N3	Cu−P[b]	N1−N2	N2−C1	N3−C1	<N3CuN1
$[(\mu\text{-abcp})(Cu(PH_3)_2)_2]^{\bullet+}$ calcd	2.020	2.091	2.269	1.337	1.369	1.377	78.5
$[(\mu\text{-abcp})(Cu(PPh_3)_2)_2]^{\bullet+}$ calcd	2.070	2.102	2.316	1.346	1.368	1.376	77.3
$[(\mu\text{-abcp})(Cu(PPh_3)_2)_2]^{\bullet+}$ exp[13]	2.045	2.098	2.263	1.345	1.363	1.360	76.6

[a] Obtained by X-ray crystallography for $[(\mu\text{-bptz})[Cu(PPh_3)_2]_2](BF_4)$ and $[(\mu\text{-abcp})[Cu(PPh_3)_2]_2](PF_6)$, respectively, cf. refs 13 and 49. [b] Cu−P distances were averaged.

SCHEME 2. Numbering Scheme of Tetrazine and Azo Complexes as Used in Table 1

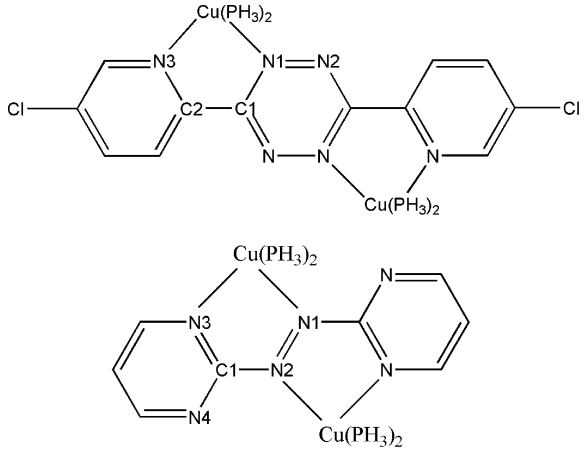

L_b (Scheme 1). Figure 1 represents isosurface plots of the spin density distributions with three different density functionals, and Table 2 provides Mulliken atomic spin densities. If we consider both metal fragments to be in a +I oxidation state, the bridging ligand must be present as a radical anion. This description of ligand-centered radical complexes is indeed borne out by the calculations, which show the spin density to be localized predominantly on the bridging ligand L. A more detailed break down into contributions from the central (tetrazine or azo) moiety and the substituent that closes the chelate ring with the metal provides more information: For the tetrazine complexes, the spin density is almost exclusively localized in the bridging tetrazine ligand, predominantly on those two nitrogen atoms that coordinate to the metal (cf. Table 2). Almost no delocalization into the pyridine or pyrimidine rings is observed. For the azo complexes, positive spin density is particularly localized at the N atoms of the bridge. For $[(\mu\text{-abpy})(Cu(PH_3)_2)_2]^{\bullet+}$ and $[(\mu\text{-abcp})(Cu(PH_3)_2)_2]^{\bullet+}$, where the azo group is substituted with pyridine, some additional spin density (positive and negative) is present on these aromatic rings, whereas the ester-substituted $[(\mu\text{-adcO}^t\text{Bu})(Cu(PH_3)_2)_2]^{\bullet+}$ shows only some small positive spin density at the oxygen atoms. In all three complexes, there is very little overall spin density at the metal but significantly more than that for the tetrazine complexes.

The dependence of the spin density distribution on the exchange-correlation functional follows the same trend in all six complexes and is consistent with previous experience for open-shell transition-metal complexes:[9,50,51] Generalized gradient approximation (GGA) functionals such as BP86 overestimate the covalency of the metal−ligand bond, and an increasing admixture of Hartree−Fock exchange renders the bonding more ionic. For systems with predominantly metal-centered spin density, this means increasing concentration of this spin density on the metal. In the present case of a ligand-centered radical, the exact-exchange admixture localizes the spin density even more on the ligand, with less metal contributions (cf. Table 2).

TABLE 2: Dependence of Mulliken Atomic Spin Densities on Exchange-Correlation Functional[a]

		Cu	azo/tetrazine (N)[b]	substituent of the chelating ligand[c]
$[(\mu\text{-bptz})(CuL_2)_2]^{\bullet+}$	BP86	0.02	0.94 (0.64)	−0.01
	B3LYP	0.01	0.98 (0.70)	−0.01
	BHLYP	0.00	1.00 (0.78)	0.00
$[(\mu\text{-bmtz})(CuL_2)_2]^{\bullet+}$	BP86	0.02	0.76 (0.58)	0.09
	B3LYP	0.00	0.88 (0.74)	0.05
	BHLYP	−0.01	0.98 (0.88)	0.01
$[(\mu\text{-bpztz})(CuL_2)_2]^{\bullet+}$	BP86	0.02	0.80 (0.62)	0.06
	B3LYP	0.01	0.94 (0.74)	0.01
	BHLYP	−0.01	0.98 (0.82)	0.00
$[(\mu\text{-abpy})(CuL_2)_2]^{\bullet+}$	BP86	0.02	0.50	0.22
	B3LYP	0.00	0.58	0.20
	BHLYP	−0.01	0.70	0.15
$[(\mu\text{-abcp})(CuL_2)_2]^{\bullet+}$	BP86	0.03	0.44	0.22
	B3LYP	0.01	0.56	0.19
	BHLYP	−0.01	0.68	0.15
$[(\mu\text{-adcO}^t\text{Bu})(CuL_2)_2]^{\bullet+}$	BP86	0.04	0.58	0.14
	B3LYP	0.02	0.68	0.12
	BHLYP	−0.01	0.80	0.10

[a] Spin densities broken down into fragment contributions from metal (values pertain to one metal only) and ligands. [b] Contribution of the tetrazine/azo moiety. For tetrazine ligands, the individual contributions of the two coordinating N atoms are also shown in parentheses. [c] Contribution from one of the attached chelating substituents of the tetrazine/azo bridging ligand.

The assignment of physical oxidation states is relatively straightforward in the title systems. Due to the predominant localization of the spin density on the bridging radical-anion ligand, a description with two Cu^I centers is undoubtedly the most useful way of viewing these complexes. We note in passing that detailed analyses of quantum chemical calculations may also provide good physical oxidation states in less clear-cut cases.[9]

Metal Hyperfine Coupling Tensors: Comparison with Experiment. Table 3 compares computed and, as far as available, experimental ^{65}Cu hyperfine coupling constants. While the spin density is mostly centered on the bridging ligand (see above), the hyperfine coupling at the metal is still appreciable, albeit of course much smaller (roughly by an order of magnitude) than for complexes with predominantly metal-centered spin density. Experimental isotropic Cu HFCs are available for two tetrazine systems $\{[(\mu\text{-bptz})(CuL_2)_2]^{\bullet+}$ and $[(\mu\text{-bmtz})(CuL_2)_2]^{\bullet+}\}$ and two azo complexes $\{[(\mu\text{-abpy})(CuL_2)_2]^{\bullet+}$ and $[(\mu\text{-adcO}^t\text{Bu})(CuL_2)_2]^{\bullet+}\}$. The sign of A_{iso} was not determined experimentally. However, our calculations provide strong indications that it is negative.

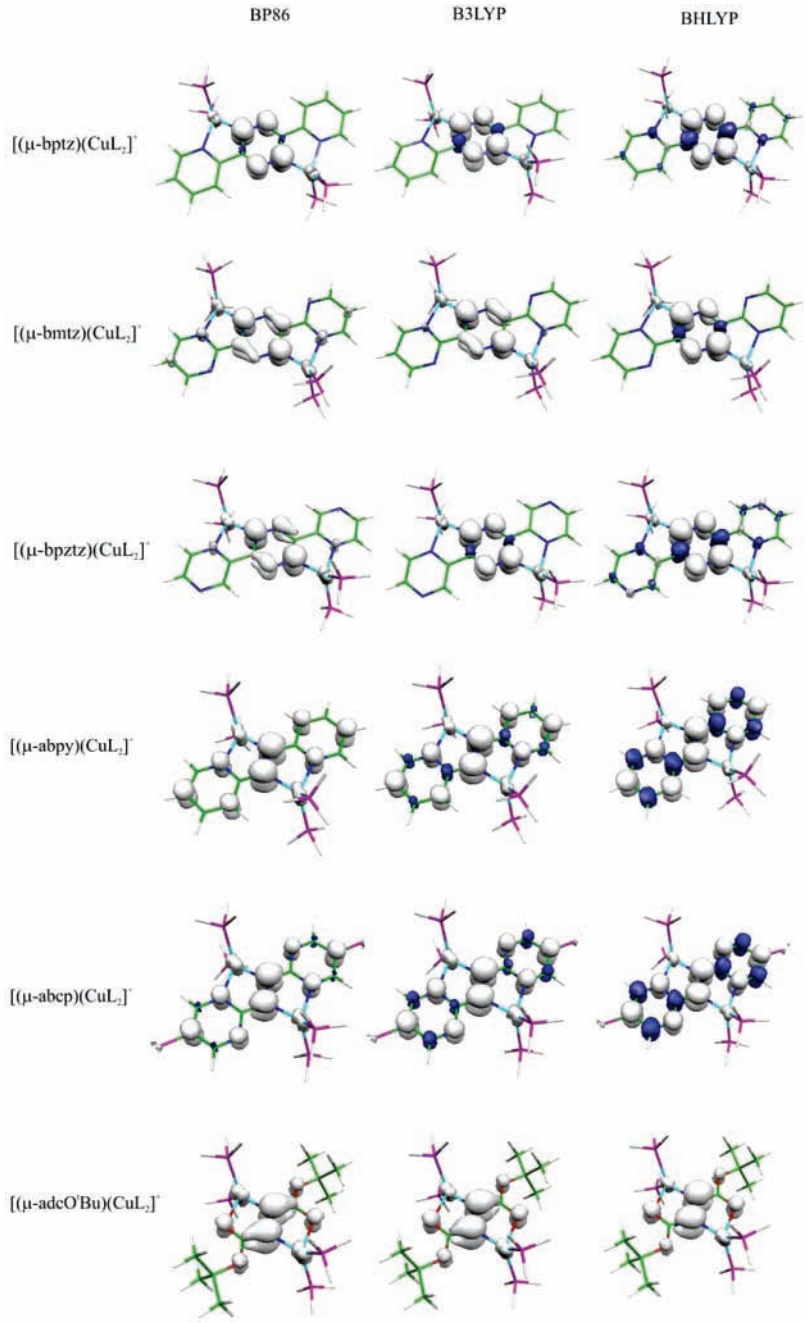

Figure 1. Isosurface plots (±0.003 au) of the spin density distribution calculated with three different functionals.

With increasing HF exchange in the functional used, the calculated A_{iso} values tend to become more negative. The isotropic FC contribution A^{FC} is negative (between −30 MHz and −50 MHz) for all complexes. SO corrections to A_{iso} (A^{PC}) are significantly smaller but nonnegligible, and they are positive. At the BP86 level, the SO corrections amount to about 15−25% of the absolute A^{FC} value. However, as exact-exchange admixture renders A^{FC} more negative and A^{PC} less positive, this ratio decreases to about 6−10% at BHLYP level. As the FC contribution dominates, the overall value of A_{iso} becomes more negative along the series BP86−B3LYP−BHLYP. This increase of the absolute value is counterintuitive: On the basis of the increasing localization of spin density on the bridging ligand with an increasing amount of HF exchange admixture, one would expect a less negative A^{FC} contribution. Detailed analyses of this unexpected behavior are provided further below.

Turning to the comparison with the experimental A_{iso} values (Table 3), we see a nonuniform performance of the different functionals: The absolute values for the tetrazine systems [(μ-bptz)$(CuL_2)_2]^{\bullet+}$ and [(μ-bmtz)$(CuL_2)_2]^{\bullet+}$ are already overestimated by the BP86 functional, and the discrepancy between theory and experiment becomes larger upon exact-exchange admixture. In contrast, the two azo systems [(μ-abpy)$(CuL_2)_2]^{\bullet+}$ and [(μ-adcO^{t}Bu)$(CuL_2)_2]^{\bullet+}$ have relatively large (negative) values, which are underestimated by the BP86 GGA functional. While the B3LYP value is closest to experiment (A^{PC} included) for [(μ-abpy)$(CuL_2)_2]^{\bullet+}$, the experimental value for [(μ-adcO^{t}Bu)$(CuL_2)_2]^{\bullet+}$ is even better reproduced by the more negative BHLYP result.

The dipolar hyperfine couplings exhibit almost axial symmetry (with small deviations especially for [(μ-bmtz)$(Cu(PH_3)_2)_2]^{\bullet+}$). Again, the SO contribution ($A^{dip,2}$) is of opposite sign compared with the primary nonrelativistic contribution (A^{dip}) and thus reduces the overall anisotropy somewhat. In contrast to the nonintuitive dependence of A^{iso} on the exchange-correlation functional (see above), the absolute values of both

TABLE 3: Computed and Experimental ^{65}Cu HFC Tensors (in MHz) for the Title Complexes

		BP86	B3LYP	BHLYP
$[(\mu\text{-bptz})(CuL_2)_2]^{\bullet+}$	A_{iso}	−31.1	−33.2	−37.2
	A^{FC}	−36.0	−36.6	−39.6
	A^{PC}	4.9	3.4	2.3
	A^{dip}	−27.5, 13.2, 14.3	−19.6, 9.4, 10.2	−13.5, 6.1, 7.4
	$A^{dip,2}$	4.1, −2.3, −1.8	2.9, −1.6, −1.4	2.1, −1.1, −1.0
	A_{iso} (exp)[10]	(−) 21.24		
$[(\mu\text{-bmtz})(CuL_2)_2]^{\bullet+}$	A_{iso}	−29.6	−34.8	−41.1
	A^{FC}	−35.2	−39.0	−43.9
	A^{PC}	5.6	4.1	2.8
	A^{dip}	−29.0, 11.2, 17.9	−22.6, 8.7, 13.9	−15.9, 5.9, 9.9
	$A^{dip,2}$	4.7, −3.0, −1.6	3.5, −2.2, −1.3	2.4, −1.4, −1.0
	A_{iso} (exp)[11]	(−) 23.09		
$[(\mu\text{-bpztz})(CuL_2)_2]^{\bullet+}$	A_{iso}	−31.7	−35.2	−38.9
	A^{FC}	−37.7	−39.2	−41.5
	A^{PC}	6.0	4.0	2.6
	A^{dip}	−31.8, 15.6, 16.2	−22.6, 11.3, 11.3	−14.9, 7.0, 7.9
	$A^{dip,2}$	5.0, −2.9, −2.1	3.5, −1.9, −1.6	2.3, −1.2, −1.1
$[(\mu\text{-abpy})(CuL_2)_2]^{\bullet+}$	A_{iso}	−30.1	−34.4	−43.0
	A^{FC}	−37.1	−39.6	−46.7
	A^{PC}	7.0	5.2	3.6
	A^{dip}	−33.0, 15.9, 17.1	−25.5, 12.3, 13.2	−18.6, 9.2, 9.4
	$A^{dip,2}$	5.3, −3.2, −2.1	4.0, −2.4, −1.6	2.6, −1.6, −1.1
	A_{iso} (exp)[10]	(−) 36.43		
$[(\mu\text{-abcp})(CuL_2)_2]^{\bullet+}$	A_{iso}	−28.2	−33.3	−41.5
	A^{FC}	−38.3	−40.5	−46.0
	A^{PC}	10.1	7.3	4.4
	A^{dip}	−40.7, 19.7, 21.0	−31.3, 15.1, 16.1	−20.9, 10.6, 10.3
	$A^{dip,2}$	7.7, −5.0, −2.7	5.8, −3.6, −2.2	3.5, −2.1, −1.4
$[(\mu\text{-adcO}^t\text{Bu})\ (CuL_2)_2]^{\bullet+}$	A_{iso}	−35.4	−40.0	−46.0
	A^{FC}	−47.9	−48.6	−50.7
	A^{PC}	12.4	8.6	4.7
	A^{dip}	−49.3, 23.8, 25.5	−36.4, 17.3, 19.1	−22.3, 10.8, 11.5
	$A^{dip,2}$	10.6, −6.0, −4.6	−4.3, −3.7, 8.0	4.4, −2.3, −2.1
	A_{iso} (exp)[10]	(−) 46.29		

A^{dip} and $A^{dip,2}$ decrease along the series BP86 > B3LYP > BHLYP, in agreement with decreasing 3d spin density upon increasing HF exchange admixture. Consequently, the ratio between $A^{dip,2}$ and A^{dip} remains roughly constant at ca. 15% in all cases.

Metal Hyperfine Couplings: Orbital Analysis. In view of the overall lower metal spin density with increasing exact-exchange admixture (cf. Figure 1), the unexpectedly more negative isotropic metal hyperfine values along the same series for all title complexes call for a closer investigation. In Table 4, A^{FC} is broken down into individual MO contributions. As has been discussed in detail earlier,[35] core-shell spin-polarization contributions to the spin density at the nucleus of a 3d complex arise from a negative 2s and a somewhat smaller positive 3s contribution (the 1s contribution has generally been found to be negligible for 3d complexes[34,35]). In the present examples, the relatively small spin density on the metal renders these contributions also relatively small, and due to similar magnitude of the 2s and 3s contributions, the overall contribution to A^{FC} from core-shell spin polarization is only between −8 and −17 MHz at the BP86 level. It decreases further with exact-exchange admixture, to values between −3 and −6 MHz at the BHLYP level.

Thus, the core-shell spin-polarization contributions become less negative, as expected, and they do not account for the bulk of the computed A^{FC}! Instead, unexpectedly, the major negative contributions come from the spin polarization of doubly occupied valence orbitals (summed up in the "VS" column of Table 4). It is these VS contributions that account for the more negative A^{FC} along the series BP86, B3LYP, and BHLYP. The predominant VS contributions arise from a few (ca. 6−10) MOs, which essentially have σ-symmetry with respect to the framework of the bridging ligands' π-system (that is, these MOs have in-plane character within the bridging ligand). All other orbitals contribute very little. Figure 2 shows for one representative case, $[(\mu\text{-bmtz})(Cu(PH_3)_2)_2]^{\bullet+}$, the spin density arising from the superposition of these orbitals. The picture may be viewed as the valence-shell spin-polarization contribution to the overall spin density distribution (cf. Figure 1). With increasing HF exchange admixture, the oscillation of spin polarization within the ligand plane becomes more notable. At the BHLYP level, appreciable negative spin density contributions have developed around the metal centers. As the MOs involved have some 4s

TABLE 4: Orbital Contributions to A^{FC}(Cu) (in MHz)

		A^{FC}	2s	3s	VS[a]	rest[b]
$[(\mu\text{-bptz})(CuL_2)_2]^{\bullet+}$	BP86	−36.0	−30.1	21.5	−30.0	2.6
	B3LYP	−36.6	−24.2	19.7	−32.8	0.7
	BHLYP	−39.6	−21.0	17.5	−40.0	3.9
$[(\mu\text{-bmtz})(CuL_2)_2]^{\bullet+}$	BP86	−32.8	−28.3	20.1	−27.6	3.0
	B3LYP	−38.0	−26.5	21.1	−38.6	6.0
	BHLYP	−45.9	−25.2	20.9	−43.9	2.3
$[(\mu\text{-bpztz})(CuL_2)_2]^{\bullet+}$	BP86	−37.7	−34.5	24.4	−30.7	3.1
	B3LYP	−39.2	−28.4	22.1	−36.0	3.1
	BHLYP	−41.5	−22.7	19.9	−42.2	3.5
$[(\mu\text{-abpy})(CuL_2)_2]^{\bullet+}$	BP86	−37.1	−35.8	25.2	−28.0	1.5
	B3LYP	−39.6	−31.5	24.9	−35.6	2.6
	BHLYP	−46.7	−28.9	24.2	−42.1	0.1
$[(\mu\text{-abcp})(CuL_2)_2]^{\bullet+}$	BP86	−38.3	−43.9	30.2	−26.9	2.3
	B3LYP	−40.5	−38.3	30.0	−39.4	7.2
	BHLYP	−46.0	−32.7	27.4	−53.4	12.7
$[(\mu\text{-adcO}^t\text{Bu})(CuL_2)_2]^{\bullet+}$	BP86	−47.9	−52.8	36.0	−32.0	0.9
	B3LYP	−48.6	−44.0	34.2	−38.0	−0.8
	BHLYP	−50.7	−34.2	28.5	−39.4	−5.6

[a] The most relevant valence-shell polarization contributions have been summed up. [b]Smaller (below a threshold of 10 MHz) valence-shell and core-shell contributions. Note that contributions coming from the SOMO are essentially negligible.

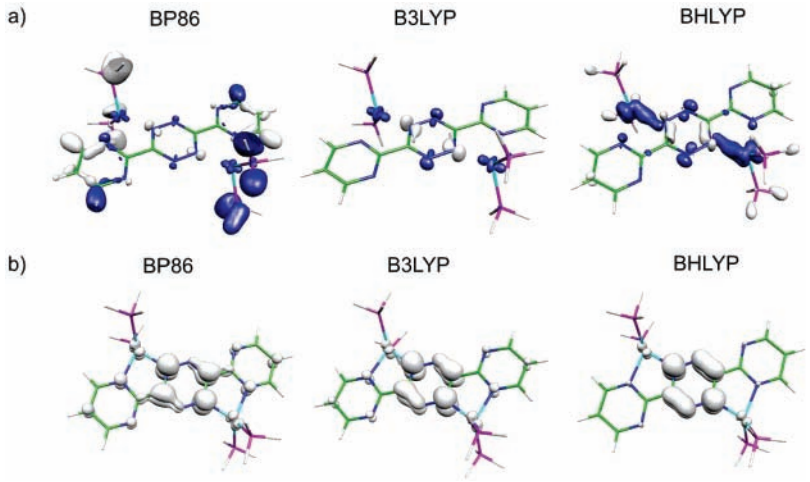

Figure 2. Isosurface plots (±0.003 au) of (a) spin-polarization contributions (sum of relevant contributions from formally doubly occupied MOs) to the spin density and (b) SOMO spin density in $[(\mu\text{-bmtz})(Cu(PH_3)_2)_2]^{\bullet+}$ for three different functionals.

TABLE 5: Natural Atomic Orbital (NAO) Occupation Numbers and Spin Populations (in parentheses) of the Metal 3d and 4s Orbitals[a]

		BP86	B3LYP	BHLYP
$[(\mu\text{-bptz})(CuL_2)_2]^{\bullet+}$	4s	0.416 (−0.0020)	0.377 (−0.0022)	0.336 (−0.0025)
	3d	9.779 (0.0265)	9.834 (0.0158)	9.872 (0.0087)
$[(\mu\text{-bmtz})(CuL_2)_2]^{\bullet+}$	4s	0.417 (−0.0019)	0.378 (−0.0024)	0.337 (−0.0030)
	3d	9.775 (0.0285)	9.825 (0.0181)	9.873 (0.0107)
$[(\mu\text{-bpztz})(CuL_2)_2]^{\bullet+}$	4s	0.417 (−0.0021)	0.378 (−0.0024)	0.337 (−0.0027)
	3d	9.777 (0.0316)	9.826 (0.0187)	9.873 (0.0096)
$[(\mu\text{-abpy})(CuL_2)_2]^{\bullet+}$	4s	0.432 (−0.0022)	0.393 (−0.0027)	0.351 (−0.0034)
	3d	9.775 (0.0343)	9.822 (0.0228)	9.871 (0.0133)
$[(\mu\text{-abcp})(CuL_2)_2]^{\bullet+}$	4s	0.427 (−0.0021)	0.388 (−0.0026)	0.346 (−0.0033)
	3d	9.769 (0.0454)	9.820 (0.0303)	9.869 (0.0164)
$[(\mu\text{-adcO}^t\text{Bu})(CuL_2)_2]^{\bullet+}$	4s	0.434 (−0.0028)	0.393 (−0.0034)	0.348 (−0.0039)
	3d	9.804 (0.0564)	9.822 (0.0361)	9.880 (0.0176)

[a] From natural population analyses (NPA[45]).

character on copper, this leads to increasing negative spin density contributions also at the metal nuclei, thus explaining the unexpected dependence of A^{FC} on the functional. This spin density obviously arises from the spin polarization of the σ-framework by the π-type semioccupied molecular orbital (SOMO) (cf. Figure 2b). We may consider this spin-polarization mechanism as the equivalent of the McConnell mechanism for π-radicals.[52] In typical π-radicals, the polarization of the σ-framework accounts for positive spin density at relevant ring nuclei (e.g., visible as positive ^{13}C HFCs) and particularly for the characteristic negative spin density at the ring protons. In the present case, the metal atoms play the role of the ring protons: The positive π-type spin density at the coordinating nitrogen atoms gives rise to a negative spin density on the Cu end of the N−Cu σ-bond. This explains the bulk of the negative spin density at the metal nuclei.

While the core-shell spin polarization depends on the metal 3d population,[34] this valence-shell spin polarization should be reflected in the metal 4s population. We expect therefore that the 3d spin population should decrease from BP86 to B3LYP to BHLYP, whereas the 4s spin population should increase along the same series. This is demonstrated by computed NPA occupations and spin populations (Table 5). With increasing HF exchange admixture, the increasing bond ionicity diminishes the "hole" in the $3d^{10}$ shell. While the 3d population thus increases, the corresponding spin population decreases. In the case of the Cu 4s orbital, the overall population decreases, again reflecting the greater ionic bonding. But at the same time, the 4s spin population becomes more negative, due to enhanced spin polarization of the σ-framework by the π-type SOMO (see above). Note that the relatively small 4s spin population influences the spin density at the copper nuclei more than the somewhat larger 3d spin population, as the 4s shell has a direct amplitude at the nucleus. We see also that the NPA spin populations (Table 5) reflect the A_{iso} values more faithfully than the gross Mulliken spin densities discussed above (Table 2).

Ligand Hyperfine Couplings. Comparison with experiment for the nitrogen hyperfine couplings is more restricted, as data are available only for $[(\mu\text{-bptz})(CuL_2)_2]^{\bullet+}$, $[(\mu\text{-bmtz})(CuL_2)_2]^{\bullet+}$, and $[(\mu\text{-adcO}^t\text{Bu})(CuL_2)_2]^{\bullet+}$ (Table 6). These couplings arise from the coordinating nitrogen of the tetrazine or azo unit and in $[(\mu\text{-bptz})(CuL_2)_2]^{\bullet+}$ and $[(\mu\text{-bmtz})(CuL_2)_2]^{\bullet+}$ also from the uncoordinated nitrogen atom of the tetrazine ring. The calculations have been performed on all six title complexes. Looking first at the azo complexes, we see that A_{iso} of the azo-nitrogen atoms increases along the series BP86 < B3LYP < BHLYP, consistent with the enhancement of spin density on the ligand by the exact-exchange admixture (Table 6). SO effects (A^{PC}) are negligible in this case and for all nitrogen HFCs in general (all values are smaller than 0.1 MHz). Compared with the only available experimental value for an azo system, $[(\mu\text{-adcO}^t\text{Bu})(CuL_2)_2]^{\bullet+}$, the BP86 result is clearly too low, whereas B3LYP and BHLYP bracket the experimental number. The dipolar contribution A^{dip} is of similar magnitude as the FC contribution and increases also with more HF exchange admixture but with a less pronounced dependence on the functional. Rather small A^{FC} and A^{dip} values are computed for the nitrogen atom of the pyridine ring in the azopyridine compounds $[(\mu\text{-abpy})(CuL_2)_2]^{\bullet+}$ and $[(\mu\text{-abcp})(CuL_2)_2]^{\bullet+}$.

TABLE 6: Computed and Experimental ^{14}N HFC Tensors (in MHz)

			N, coord, tetrazine	N, uncoord, tetrazine	N, coord, pyrimidine
$[(\mu\text{-bptz})(CuL_2)_2]^{\bullet+}$		A_{iso} (exp)[10]	16.96	12.96	
		A_{iso}	10.3	2.8	−0.2
	BP86	A^{FC}	10.4	2.9	−0.2
		A^{dip}	−16.3, −15.9, 32.2	−8.5, −8.0, 16.5	−0.3, 0.0, 0.3
		A_{iso}	17.5	8.1	−0.8
	B3LYP	A^{FC}	17.6	8.1	−0.8
		A^{dip}	−18.0, −17.6, 35.6	−11.1, −10.4, 21.5	−0.8, 0.2, 0.6
		A_{iso}	27.9	15.4	−2.4
	BHLYP	A^{FC}	28.0	15.4	−2.4
		A^{dip}	−19.9, −19.2, 39.1	−13.8, −12.7, 26.5	−2.6, 1.1, 1.5
$[(\mu\text{-bmtz})(CuL_2)_2]^{\bullet+}$		A_{iso} (exp)[11]	17.07	13.62	
		A_{iso}	10.1	−0.8	0.7
	BP86	A^{FC}	10.2	−0.8	0.7
		A^{dip}	−15.0, −14.6, 29.6	−1.9, −0.9, 2.8	−1.7, −1.5, 3.2
		A_{iso}	18.8	0.7	0.5
	B3LYP	A^{FC}	18.9	0.7	0.5
		A^{dip}	−18.6, −18.2, 36.8	−3.5, −2.6, 6.1	−1.1, −0.8, 1.9
		A_{iso}	31.2	5.4	−0.8
	BHLYP	A^{FC}	31.2	5.4	−0.8
		A^{dip}	−21.8, −21.1, 42.9	−6.8, −5.8, 12.6	−0.5, 0.1, 0.4
$[(\mu\text{-bpztz})(CuL_2)_2]^{\bullet+}$		A_{iso}	10.3	0.8	0.5
	BP86	A^{FC}	10.4	0.9	0.5
		A^{dip}	−15.8, −15.4, 31.2	−4.9, −4.3, 9.1	−1.3, −1.1, 2.4
		A_{iso}	18.5	5.0	−0.3
	B3LYP	A^{FC}	18.6	5.0	−0.2
		A^{dip}	−18.7, −18.2, 36.9	−7.9, −7.2, 15.2	−0.3, 0.0, 0.3
		A_{iso}	29.3	12.4	−2.4
	BHLYP	A^{FC}	29.4	12.4	−2.4
		A^{dip}	−20.8, −20.0, 40.9	−11.7, −10.6, 22.3	−2.5, 1.1, 1.4

			N, azo	N, py
$[(\mu\text{-abpy})(CuL_2)_2]^{\bullet+}$	BP86	A_{iso}	6.2	2.4
		A^{FC}	6.3	2.5
		A^{dip}	−12.4, −12.4, 24.8	−4.0, −3.9, 7.9
	B3LYP	A_{iso}	12.5	4.4
		A^{FC}	12.5	4.5
		A^{dip}	−14.8, −14.8, 29.6	−4.7, −4.5, 9.2
	BHLYP	A_{iso}	21.9	9.0
		A^{FC}	22.0	9.1
		A^{dip}	−17.6, −17.2, 34.8	−6.3, −6.0, 12.3
$[(\mu\text{-abcp})(CuL_2)_2]^{\bullet+}$	BP86	A_{iso}	5.1	2.4
		A^{FC}	5.2	2.4
		A^{dip}	−11.3, −11.3, 22.6	−4.1, −4.0, 8.0
	B3LYP	A_{iso}	10.9	4.5
		A^{FC}	11.1	4.5
		A^{dip}	−13.9, −13.9, 27.8	−4.9, −4.7, 9.6
	BHLYP	A_{iso}	19.8	9.3
		A^{FC}	19.9	9.3
		A^{dip}	−16.9, −16.6, 33.5	−6.7, −6.4, 13.1
$[(\mu\text{-adcO}^t\text{Bu})\ (CuL_2)_2]^{\bullet+}$		A_{iso} (exp)[10]	17.94	
	BP86	A_{iso}	6.6	
		A^{FC}	6.8	
		A^{dip}	−14.5, −14.6, 29.1	
	B3LYP	A_{iso}	13.5	
		A^{FC}	13.7	
		A^{dip}	−17.1, −17.2, 34.4	
	BHLYP	A_{iso}	23.2	
		A^{FC}	23.3	
		A^{dip}	−20.0, −19.8, 39.8	

Within the series of the tetrazine compounds, we may evaluate both the coordinating and noncoordinating tetrazine nitrogen atoms. The coordinated nitrogen atom of the pyridine ring exhibits almost vanishing A^{FC} and A^{dip} values, consistent with the lack of experimental observation. Starting with the coordinating tetrazine nitrogen HFCs for $[(\mu\text{-bptz})(CuL_2)_2]^{\bullet+}$ and $[(\mu\text{-bmtz})(CuL_2)_2]^{\bullet+}$, the computations show again an increase with exact-exchange admixture. In both cases, the B3LYP result agrees excellently with experiment. A^{dip} is of the same order of magnitude and shows the same dependence on the functional.

Matters turn out to be more complicated for the noncoordinating tetrazine nitrogen isotropic HFCs, which are available experimentally for $[(\mu\text{-bptz})(CuL_2)_2]^{\bullet+}$ and $[(\mu\text{-bmtz})(CuL_2)_2]^{\bullet+}$. For the bptz ligand, the computed values increase dramatically with exact-exchange admixture and the experimental value is again bracketed by the B3LYP and BHLYP results (note that the HFCs remain lower than those for the coordinated nitrogen atoms). On the other hand, the experimentally even slightly larger value for the bmtz system is not reproduced so well by the calculations. The BP86 and B3LYP values are only slightly negative and slightly positive, respectively. Only at the BHLYP level is an appreciably positive value obtained but at the expense of overshooting for the coordinating nitrogen atom (Table 6). These results are consistent with the computed spin density

TABLE 7: Computed ^{14}N A_{iso} Values (in MHz) for Free Tetrazine Radical Anions

		N1 (ring)	N2 (ring)	N (substituent)
bptz$^{\bullet-}$	BP86	6.9	−0.7	0.7
	B3LYP	15.7	1.9	0.7
	BHLYP	26.2	12.7	−2.1
bmtz$^{\bullet-}$	BP86	0.8	0.8	0.7
	B3LYP	1.2	1.2	2.3
	BHLYP	1.4	1.4	6.0
bpztz$^{\bullet-}$	BP86	5.8	−1.9	2.6
	B3LYP	13.4	−1.4	1.5
	BHLYP	28.1	3.7	−0.1

distributions, which signal appreciable spin density (increasing with exact-exchange admixture) on the noncoordinating tetrazine nitrogen for the bptz and bpztz systems but much lower values for the bmtz complex (cf. Figure 1).

This slight difference between the bmtz compound and the bptz and bpztz systems is already present for the free ligand radical anions. Table 7 shows HFC tensor results for the nitrogen atoms in the free ligands (only those N atoms are considered which are relevant in the complexes). While the optimization gave C_{2h}-symmetrical structures for bptz$^{\bullet-}$ and bpztz$^{\bullet-}$ (with two distinct pairs of nirtogen atoms within the tetrazine ring), a D_{2h}-symmetrical structure was obtained for bmtz$^{\bullet-}$ (with four equivalent nitrogen atoms in the tetrazine moiety and two equivalent nitrogen atoms in each pyrimidine). The dependence of the nitrogen HFCs on the functional for bptz$^{\bullet-}$ and bpztz$^{\bullet-}$ (Table 7) is similar to that observed in the complexes (cf. Table 6). The isotropic HFC values (A_{iso}) of both nitrogen atoms within the tetrazine ring are enhanced upon increasing exact-exchange admixture (overall, A_{iso} is larger in the complex). In contrast, bmtz$^{\bullet-}$ exhibits very low A_{iso} values and only little change for the tetrazine nitrogen atoms with increasing exact-exchange admixture (but an overall higher value and an increase with exact exhange at the nitrogen atoms of the pyrimidine substituent). This reflects a more pronounced delocalization of spin density into the substituents (cf. spin density plots for the free ligands in Figure S1 in the Supporting Information), possibly due to the more symmetrical nature of bmtz$^{\bullet-}$ compared with the other two tetrazine radical anions.

g-Tensors: Comparison with Experiment and Dependence on Functional. Tables 8 and 9 show calculated and (where available) experimental **g**-tensors for the copper complexes and the free ligand radical anions, respectively. Let us start with a brief survey of the experimental **g**-tensors, which are available from high-field EPR for five of our six title complexes. Consistent with the predominantly ligand-centered spin density (see above), the **g**-tensor anisotropy is much smaller for all complexes than for typical Cu^{II} d^9 systems (indeed, high-field EPR is necessary for a resolution of the **g**-tensor in these systems, due to the relatively low anisotropy). But, at least for the azo complexes, the anisotropy is still significantly larger than that expected for the free π-radicals (cf. below). The anisotropy for the tetrazine complexes is lower, suggesting less involvement of metal spin−orbit coupling. This is in turn also consistent with the experimentally somewhat less negative A_{iso} (Table 3) and with the somewhat smaller metal 3d spin population (Table 5). Note that only a larger 3d spin population (cf. Table 5) is expected to contribute to the **g**-tensor anisotropy, whereas copper spin−orbit coupling is not affected by the 4s spin populations. Lower 3d spin populations and **g**-tensor anisotropies in such ligand-centered radicals are typically associated with a less pronounced π-acceptor character of the bridging ligand.[14] In the present examples, the tetrazine ligands are the weaker π-acceptors. Within the set of azo ligands, abcp is known to be the best π-acceptor. Consequently, it shows the largest g anisotropy (Table 8) and 3d spin population (Table 5). The experimental **g**-tensors for the tetrazine-bridged systems have one component (g_{33}), which is relatively close to the free-electron value $g_e = 2.002319$, and the reported tensor exhibits axial symmetry, with the identical components g_{11} and g_{22} not very far above g_e. The azo-bridged complexes exhibit rhombic spectra, with g_{33} below g_e and both g_{11} and g_{22} appreciably above g_e.

Let us now turn to the computed **g**-tensors (Table 8). With increasing HF exchange admixture, the g anisotropy decreases, consistent with the enhanced ionicity of the Cu−L bond and with the resulting lower metal 3d spin populations (Table 4). We have observed this behavior earlier for complexes with ligand-centered spin density,[8,9] whereas the opposite trend holds for metal-centered spin.[28,53] The overall agreement with experiment is generally better for the present Cu complexes than that for our previous work on 4d or 5d ligand-centered sytems.[8,9]

TABLE 8: Computed and Experimental g-Tensors for the Title Complexes[a]

		g_{iso} (Δg_{iso})	g_{11} (Δg_{11})	g_{22} (Δg_{22})	g_{33} (Δg_{33})	$\Delta g_{11} - \Delta g_{33}$
[(μ-bptz)(CuL_2)$_2$]$^{\bullet+}$	exp[14]	2.0053 (3.0)	2.0067 (4.4)	2.0067 (4.4)	2.0026 (0.3)	4.1
	BP86	2.0043 (2.0)	2.0091 (6.8)	2.0076 (5.3)	1.9962 (−6.1)	12.9
	B3LYP	2.0041 (1.8)	2.0072 (4.9)	2.0060 (3.7)	1.9992 (−3.1)	8.0
	BHLYP	2.0040 (1.7)	2.0064 (4.1)	2.0047 (2.4)	2.0008 (−1.5)	5.6
[(μ-bmtz)(CuL_2)$_2$]$^{\bullet+}$	exp[11]	2.0048 (2.5)	2.0062 (3.9)	2.0062 (3.9)	2.0021 (−0.2)	4.1
	BP86	2.0033 (1.0)	2.0123 (10.0)	2.0066 (4.3)	1.9910 (−11.3)	21.3
	B3LYP	2.0030 (0.7)	2.0080 (5.7)	2.0055 (3.2)	1.9955 (−6.8)	14.5
	BHLYP	2.0033 (1.0)	2.0062 (3.9)	2.0045 (2.2)	1.9991 (−3.2)	7.1
[(μ-bpztz)(CuL_2)$_2$]$^{\bullet+}$	BP86	2.0034 (1.1)	2.0115 (9.2)	2.0077 (5.4)	1.9910 (−11.3)	20.5
	B3LYP	2.0036 (1.3)	2.0080 (5.7)	2.0063 (4.0)	1.9964 (−5.9)	11.6
	BHLYP	2.0037 (1.4)	2.0065 (4.2)	2.0049 (2.6)	1.9997 (−2.6)	6.8
[(μ-abpy)(CuL_2)$_2$]$^{\bullet+}$	exp[10]	2.0050 (2.7)	2.0134 (11.1)	2.0047 (2.4)	1.9968 (−5.5)	16.6
	BP86	2.0053 (3.0)	2.0142 (11.9)	2.0053 (3.0)	1.9964 (−5.9)	17.8
	B3LYP	2.0041 (1.8)	2.0107 (8.4)	2.0046 (2.3)	1.9971 (−5.2)	13.6
	BHLYP	2.0034 (1.1)	2.0079 (5.6)	2.0041 (1.8)	1.9982 (−4.1)	9.7
[(μ-abcp)(CuL_2)$_2$]$^{\bullet+}$	exp[13]	2.0077 (5.4)	2.016 (13.7)	2.007 (4.7)	1.998 (−4.3)	18.0
	BP86	2.0091 (6.8)	2.0224 (20.1)	2.0089 (6.6)	1.9963 (−6.0)	26.1
	B3LYP	2.0066 (4.3)	2.0163 (14.0)	2.0071 (4.8)	1.9965 (−5.8)	19.8
	BHLYP	2.0049 (2.6)	2.0109 (8.6)	2.0061 (3.8)	1.9976 (−4.7)	13.3
[(μ-adcO^{t}Bu)(CuL_2)$_2$]$^{\bullet+}$	exp[10]	2.0110 (8.7)	2.0220 (19.7)	2.0090 (6.7)	2.0020 (−0.3)	20.0
	BP86	2.0123 (10.0)	2.0235 (21.2)	2.0107 (8.4)	2.0027 (0.4)	21.6
	B3LYP	2.0083 (6.0)	2.0163 (14.0)	2.0077 (5.4)	2.0008 (−1.5)	15.5
	BHLYP	2.0050 (2.7)	2.0099 (7.6)	2.0049 (2.6)	2.0002 (−2.1)	9.7

[a] Absolute **g**-tensor components with g-shift components (deviations from g_e in ppt) in parentheses. Results with L = PH_3.

TABLE 9: Computed and Experimental *g*-Shift Tensors (in ppt) for the Free Ligand Radical Anions

		Δg_{iso}	Δg_{11}	Δg_{22}	Δg_{33}	$\Delta g_{11} - \Delta g_{33}$
bptz$^{\bullet-}$	BP86	1.1	2.2	1.1	0.0	2.2
	B3LYP	1.5	2.7	1.6	0.1	2.8
	BHLYP	1.8	3.2	2.2	0.1	3.3
bmtz$^{\bullet-}$	exp[11]	1.7				
	BP86	0.4	1.6	0.0	−0.3	1.9
	B3LYP	0.4	1.7	0.0	−0.5	2.2
	BHLYP	0.5	1.9	0.0	−0.5	2.4
bpztz$^{\bullet-}$	BP86	1.1	2.1	1.0	0.0	2.1
	B3LYP	1.2	2.4	1.2	0.1	2.5
	BHLYP	1.7	3.2	1.9	0.1	3.3
abcp$^{\bullet-}$	exp[8]	2.1				
	BP86	2.4	6.1	1.3	−0.2	6.3
	B3LYP	2.4	6.2	1.3	−0.2	6.4
	BHLYP	2.7	6.7	1.5	−0.2	6.9
abpy$^{\bullet-}$	exp[8,13]	1.8				
	BP86	1.6	4.2	0.5	0.0	4.2
	B3LYP	1.7	4.6	0.5	0.0	4.6
	BHLYP	1.9	5.1	0.5	0.0	5.1
adcO^{t}Bu$^{\bullet-}$	BP86	2.8	7.3	1.1	−0.1	7.4
	B3LYP	2.8	7.5	1.1	−0.1	7.6
	BHLYP	2.8	7.5	1.1	−0.1	7.6

For the azo complexes, both BP86 and B3LYP results may be considered to agree well with experiment for all three tensor components and thus also for the anisotropy. The BHLYP results exhibit too low g_{11} and g_{22} values and thus underestimate the *g* anisotropy.

For the two tetrazine complexes $[(\mu\text{-bptz})(CuL_2)_2]^{\bullet+}$ and $[(\mu\text{-bmtz})(CuL_2)_2]^{\bullet+}$, for which **g**-tensor data are available, the agreement between theory and experiment is less favorable: Δg_{33} is computed too negative at the BP86 level and slowly moves toward better agreement with the very small absolute experimental values upon going toward BHLYP. Also, the axial symmetry (i.e., $g_{11} = g_{22}$) of the experimental data is not reproduced by the calculations, which exhibit a splitting of ca. 1−5 ppt between the two larger components, depending on the system and functional (Table 8). Comparison of the average of the computed g_{11} and g_{22} values with the experimental value would suggest again the best agreement with experiment at the B3LYP level. On the other hand, the less negative g_{33} brings the *g* anisotropy into better agreement with experiment at the BHLYP level. However, it appears possible that the $g_{11}-g_{22}$ asymmetry was just too small to be resolved under the experimental conditions. We can also not exclude that the discrepancy between theory and experiment for g_{33} may be partly due to an insufficient magnetic-field calibration under the experimental setup (this is known to be difficult in many high-field EPR studies, and such technical limitations will affect all three tensor components in the same direction). One should thus probably not overinterpret the discrepancies between theory and experiment for the two tetrazine title complexes.

Table 9 shows computed *g*-shift tensors for the free ligand radical anions. As one might expect for typical organic π-radicals, the anisotropies are much reduced compared with the complexes, with g_{33} (the component perpendicular to the molecular plane) near g_e and g_{11} and g_{22} about 2−7 ppt above g_e, depending on the spin densities on nitrogen centers, which are responsible for the predominant spin−orbit contributions in the free radical anions. The much less pronounced dependence of the computed **g**-tensors on the exchange-correlation functional for the free ligands compared with the complexes (cf. Table 8) is notable. This confirms the above discussion of the dependence of metal−ligand covalency on the functional and of the influence of this covalency on the metal spin density. For three cases (bmtz$^{\bullet-}$, abcp$^{\bullet-}$, and abpy$^{\bullet-}$), experimental g_{iso} values are available. Only the tetrazine system, bmtz$^{\bullet-}$, appears to be reproduced most poorly by the calculations, whereas the two values of the azo compounds exhibit reasonable agreement between theory and experiment. It is furthermore clear that the azo systems exhibit more rhombic **g**-tensors, with larger g_{11} values , than the tetrazine radical anions. This reflects appreciable spin density on the nitrogen atoms of the azo bridge. The trends of **g**-tensor anisotropy in the complexes (Table 8) do not generally follow those of the free radical anions. This indicates the importance of metal−ligand interactions (related to the π-acceptor character of the free neutral ligand) for the **g**-tensor anisotropy in the complexes. On the other hand, the generally larger anisotropy for the azo compared with tetrazine systems already indicates for the free ligands some influence of the inherent spin density properties (nodes in the relevant valence orbitals) of the corresponding π-systems.

Effect of the Phosphine Coligands, Comparison of L = PH_3 and L = PPh_3. As indicated by the structural results (see above), the choice of L = PH_3 appears to be a reasonable one, partly due to a compensation between computational errors and substituent effects on structures. To nevertheless obtain an impression of the actual influence of more realistically substituted phosphine coligands, we have carried out additional calculations with triphenylphosphine ligands for two tetrazine complexes $[(\mu\text{-bptz})(CuL_2)_2]^{\bullet+}$ and $[(\mu\text{-bmtz})(CuL_2)_2]^{\bullet+}$ and one azo complex $[(\mu\text{-abcp})CuL_2)_2]^{\bullet+}$. This choice was based on the fact that these three systems indeed were studied experimentally with PPh_3 coligands. Due to system size, we restrict the calculations to one computational level, using the BP86 GGA functional. Results of such comparisons for all relevant EPR parameters are provided in Table 10. We will not compare these with experiment at this computational level but refer the reader to the corresponding experimental values in Tables 3, 6, and 8 above.

Starting with metal HFCs, we see slightly less negative A_{iso} values when PH_3 is replaced by PPh_3. For the two tetrazine complexes, this is due to a less negative FC term, whereas a more positive pseudocontact term overcompensates the slightly more negative contact term for the azo complex (Table 10). The dipolar coupling constants exhibit an unclear trend, with enhancement for the azo complex $[(\mu\text{-abcp})Cu(PPh_3)_2)_2]^{\bullet+}$, decrease for $[(\mu\text{-bmtz})(CuL_2)_2]^{\bullet+}$, and relatively little change for $[(\mu\text{-bptz})(CuL_2)_2]^{\bullet+}$. The HFC rhombicity is increased upon substitution. This probably reflects the slightly twisted ring planes in the complexes with triphenylphosphine coligands (see above). Overall these results indicate that the spin density at the metal is influenced only moderately and in a subtle fashion by the presence of the phenyl substituents.

Substituent effects on the nitrogen HFC tensors are moderate (Table 10). In all three systems, both isotropic HFC and anisotropy of the coordinating tetrazine or aza nitrogen atoms are reduced somewhat upon substitution, consistent with reduced spin density in these positions (probably reflecting some transfer of spin density to the metal, see above). The effect is by far the most pronounced for the bmtz system. The results for the noncoordinating tetrazine nitrogens are less clear-cut (but here the BP86 functional does not perform particularly well, see above). Moderate effects are found in the coordinating pyrimidine nitrogen atoms.

Substituent effects on the **g**-tensor are rather moderate for the two tetrazine complexes, resulting in a slightly increased *g* anisotropy. The effects are more pronounced for the already larger *g* anisotropy of the azo complex: All three components become more positive, leading to a larger g_{iso}. Moreover, the

TABLE 10: Comparison of EPR Parameters for Complexes with L = PH_3 and L = PPh_3[a]

Cu HFC-tensor (in MHz)

	A_{iso}	A^{FC}	A^{PC}	A^{dip}	$A^{dip,2}$
[(μ-bptz)($Cu(PH_3)_2$)$_2$]$^{\bullet+}$	−31.1	−36.0	4.9	−27.5, 13.2, 14.3	4.1, −2.3, −1.8
[(μ-bptz)($Cu(PPh_3)_2$)$_2$]$^{\bullet+}$	−26.0	−31.7	5.7	−27.7,12.6, 15.1	5.1, −2.2, −2.9
[(μ-bmtz)($Cu(PH_3)_2$)$_2$]$^{\bullet+}$	−29.6	−35.2	5.6	−29.0, 11.2, 17.9	4.7, −3.0, −1.6
[(μ-bmtz)($Cu(PPh_3)_2$)$_2$]$^{\bullet+}$	−17.8	−22.6	4.8	−20.2,4.5, 15.7	3.9, −3.4, −0.5
[(μ-abcp)($Cu(PH_3)_2$)$_2$]$^{\bullet+}$	−28.2	−38.3	10.1	−40.7, 19.7, 21.0	7.7, −5.0, −2.7
[(μ-abcp)($Cu(PPh_3)_2$)$_2$]$^{\bullet+}$	−24.9	−40.3	15.4	−50.2, 13.9, 36.3	12.0, −2.0, −10.0

N-HFC (coordinating aza/tetrazine N) (in MHz)

	A_{iso}	A^{FC}	A^{dip}
[(μ-bptz)($Cu(PH_3)_2$)$_2$]$^{\bullet+}$	10.3	10.4	−16.3, −15.9, 32.2
[(μ-bptz)($Cu(PPh_3)_2$)$_2$]$^{\bullet+}$	8.8	8.9	−14.4, −14.1, 28.5
[(μ-bmtz)($Cu(PH_3)_2$)$_2$]$^{\bullet+}$	10.1	10.2	−15.0, −14.6, 29.6
[(μ-bmtz)($Cu(PPh_3)_2$)$_2$]$^{\bullet+}$	5.3	5.3	−7.3, −7.5, 14.8
[(μ-abcp)($Cu(PH_3)_2$)$_2$]$^{\bullet+}$	5.1	5.2	−11.3, −11.3, 22.6
[(μ-abcp)($Cu(PPh_3)_2$)$_2$]$^{\bullet+}$	4.8	5.0	−10.2, −10.2, 20.4

N-HFC (uncoordinating tetrazine N) (in MHz)

	A_{iso}	A^{FC}	A^{dip}
[(μ-bptz)($Cu(PH_3)_2$)$_2$]$^{\bullet+}$	2.8	2.9	−8.5, −8.0, 16.5
[(μ-bptz)($Cu(PPh_3)_2$)$_2$]$^{\bullet+}$	5.1	5.1	−11.9, −11.5, 23.4
[(μ-bmtz)($Cu(PH_3)_2$)$_2$]$^{\bullet+}$	−0.8	−0.8	−1.9, −0.9, 2.8
[(μ-bmtz)($Cu(PPh_3)_2$)$_2$]$^{\bullet+}$	−1.7	−1.7	−2.9, 1.3, 1.6

N-HFC (coordinating, pyrimidine) (in MHz)

	A_{iso}	A^{FC}	A^{dip}
[(μ-bptz)($Cu(PH_3)_2$)$_2$]$^{\bullet+}$	−0.2	−0.2	−0.3, 0.0, 0.3
[(μ-bptz)($Cu(PPh_3)_2$)$_2$]$^{\bullet+}$	−0.4	−0.4	−0.5, 0.1, 0.4
[(μ-bmtz)($Cu(PH_3)_2$)$_2$]$^{\bullet+}$	0.7	0.7	−1.7, −1.5, 3.2
[(μ-bmtz)($Cu(PPh_3)_2$)$_2$]$^{\bullet+}$	1.8	1.8	−3.1, −3.0, 6.1
[(μ-abcp)($Cu(PH_3)_2$)$_2$]$^{\bullet+}$	2.4	2.4	−4.1, −4.0, 8.0
[(μ-abcp)($Cu(PPh_3)_2$)$_2$]$^{\bullet+}$	2.2	2.3	−3.6, −3.6, 7.3

g-tensor[b]

	g_{iso} (Δg_{iso})	g_{11} (Δg_{11})	g_{22} (Δg_{22})	g_{33} (Δg_{33})	$\Delta g_{11} - \Delta g_{33}$
[(μ-bptz)($Cu(PH_3)_2$)$_2$]$^{\bullet+}$	2.0043 (2.0)	2.0091 (6.8)	2.0076 (5.3)	1.9962 (−6.1)	12.9
[(μ-bptz)($Cu(PPh_3)_2$)$_2$]$^{\bullet+}$	2.0059 (3.6)	2.0114 (9.1)	2.0088 (6.5)	1.9977 (−4.6)	13.7
[(μ-bmtz)($Cu(PH_3)_2$)$_2$]$^{\bullet+}$	2.0033 (1.0)	2.0123 (10.0)	2.0066 (4.3)	1.9910 (−11.3)	21.3
[(μ-bmtz)($Cu(PPh_3)_2$)$_2$]$^{\bullet+}$	2.0027 (0.4)	2.0128 (10.5)	2.0054 (3.1)	1.9899 (−12.4)	22.9
[(μ-abcp)($Cu(PH_3)_2$)$_2$]$^{\bullet+}$	2.0091 (6.8)	2.0224 (20.1)	2.0089 (6.6)	1.9963 (−6.0)	26.1
[(μ-abcp)($Cu(PPh_3)_2$)$_2$]$^{\bullet+}$	2.0149 (12.6)	2.0314 (29.1)	2.0126 (10.3)	2.0006 (−1.7)	30.8

[a] BP86 results. For L = PPh_3, DZ basis sets[33] were used for the C and H atoms of the triphenylphosphine ligands. [b] Absolute **g**-tensor components with *g*-shift components (deviations from g_e in ppt) in parentheses.

anisotropy is also enhanced, mainly due to the considerably larger g_{11} value (Table 10). A possible influence on the *g* anisotropy due to competition between coligands and bridging radical-anion ligand for back-bonding from metal orbitals has been pointed out by Kaim et al.[14] However, a straightforward argument via attenuation of the Cu(I) $d_\pi \rightarrow p^*$(tetrazine) back-donation by a competing better π-acceptor PPh_3 vs PH_3 does not fit the computed data in the present examples. In that case, the better π-acceptor triphenylphosphine coligands should reduce the *g* anisotropy whereas a slight enhancement is found. It appears that structural changes (in particular the slight twisting of the bridging ligand planes due to the steric requirements of the larger coligands, see above) mask the moderate electronic influences.

Molecular-Orbital and Atomic Spin−Orbit Analyses of g-Tensors. For further analyses of the interrelations between electronic structure and **g**-tensors, we used two analysis tools implemented within our MAG-ReSpect code. First, we broke down the dominant $\Delta g_{SO/OZ}$ part of the *g*-shift tensor (eq 6) into atomic contributions coming exclusively from specific atoms. This is possible due to the atomic nature of the atomic meanfield SO operators h_{SO} which we employed. They allow it to switch SO operators on or off for individual atoms. Here, we have used SO operators only for Cu or N atoms and switched them off for the remaining atoms.

Table 11 shows the result of the break down of the $\Delta g^{SO/OZ}$ contribution of the g-shift tensor (BP86 results in ppt) into Cu and N contributions for all six complexes (the Cu contributions are also shown for the three complexes with L = PPh_3). As expected, the dominant contributions arise from copper spin−orbit coupling. However, their fraction of the total $\Delta g^{SO/OZ}$ ranges only from 61% to 83% for g_{11} and g_{22}. This indicates a significant ligand spin−orbit contribution to $\Delta g^{SO/OZ}$. Closer analysis shows that it is mainly the coordinating nitrogen atoms of the tetrazine ring or azo group, respectively, which provide ligand contributions (some further contributions result from the other nitrogen atoms and, for [(μ-abcp)(CuL_2)$_2$]$^{\bullet+}$ and [(μ-adcO^t-Bu)(CuL_2)$_2$]$^{\bullet+}$, from chlorine and oxygen atoms). Only the deviations of the g_{33} component from g_e are almost entirely due to copper spin−orbit coupling. This may be rationalized by vanishing spin−orbit contributions into the out-of-plane direction in the free π-radicals (cf. Table 9). Indeed, the SOMO in the complexes is still mainly of ligand-centered π-character (cf. SOMO spin density in Figure 2b), and only spin−orbit

TABLE 11: Breakdown of the $\Delta g^{SO/OZ}$ Contribution of the *g*-Shift Tensor (in ppt) into Cu and N Contributions[a]

	Cu			coordinating N (tetrazine/azo)		
	Δg_{11}	Δg_{22}	Δg_{33}	Δg_{11}	Δg_{22}	Δg_{33}
$[(\mu\text{-bptz})(Cu(PH_3)_2)_2]^{\bullet+}$	4.5 (66%)	3.3 (62%)	−6.1 (97%)	1.6 (24%)	0.8 (15%)	0.0
$[(\mu\text{-bptz})(Cu(PPh_3)_2)_2]^{\bullet+}$	6.7 (74%)	4.4 (68%)	−4.3 (99%)	1.2 (13%)	0.5 (8%)	0.0
$[(\mu\text{-bmtz})(Cu(PH_3)_2)_2]^{\bullet+}$	7.9 (79%)	3.1 (74%)	−11.3 (99%)	1.4 (14%)	0.7 (17%)	0.0
$[(\mu\text{-bmtz})(Cu(PPh_3)_2)_2]^{\bullet+}$	8.8 (84%)	2.8 (93%)	−12.1 (97%)	1.1 (10%)	0.2 (7%)	0.0
$[(\mu\text{-bpztz})(Cu(PH_3)_2)_2]^{\bullet+}$	7.0 (76%)	3.6 (67%)	−11.3 (99%)	1.5 (16%)	0.8 (15%)	0.0
$[(\mu\text{-abpy})(Cu(PH_3)_2)_2]^{\bullet+}$	9.3 (78%)	1.9 (66%)	−6.0 (98%)	2.0 (17%)	0.4 (14%)	0.0
$[(\mu\text{-abcp})(Cu(PH_3)_2)_2]^{\bullet+}$	15.0 (75%)	4.0 (61%)	−5.9 (98%)	2.0 (10%)	0.4 (6%)	0.0
$[(\mu\text{-abcp})(Cu(PPh_3)_2)_2]^{\bullet+}$	29.0 (87%)	10.2 (84%)	−1.9 (95%)	1.5 (5%)	0.4 (3%)	0.0
$[(\mu\text{-adcO}^t\text{Bu})(Cu(PH_3)_2)_2]^{\bullet+}$	17.0 (80%)	7.0 (83%)	0.5 (99%)	2.5 (12%)	0.4 (5%)	0.0

[a] Results for the BP86 functional, common gauge on metal center. SO operators "switched on" only for those atoms which are indicated. Numbers in parentheses represent the fraction of the specific contributions to the total $\Delta\mathbf{g}^{SO/OZ}$.

contributions from copper remain in g_{33} direction. For the three complexes with L = PPh_3, the g_{11} and g_{22} contributions are 5−20% higher compared with L = PH_3, indicating a more pronounced copper spin−orbit coupling (and thus a slightly larger metal 3d spin density, see above).

The second analysis tool used is the break down of $\Delta g_{SO/OZ}$ into individual couplings ("excitations") between occupied and vacant MOs within the sum-over-states expression (eq 7).[54] As this is particularly straightforward for nonhybrid functionals, where the equations are not coupled by HF exchange terms, we refer in the following to the BP86 results.

The analyses show excitations from doubly occupied MOs with β-spin to the β-component of the SOMO to dominate the **g**-tensor for the azo complexes (between +14 and +27 ppt for the largest component Δg_{11}). The corresponding excitations contribute less (between +5 and +8 ppt) for the tetrazine complexes. This reflects the larger metal character of these doubly occupied MOs for the azo systems, connected to their more pronounced π-acceptor ability. Excitations from SOMO to virtual MOs (with α-spin) contribute negatively to g_{11}, between −4 and −9 ppt for both azo and tetrazine ligands. The relatively large positive Δg_{11} values for the azo complexes and the small Δg_{11} values for the tetrazine systems result.

For Δg_{22} and Δg_{33}, the interplay between the different kinds of excitations is more subtle and may be analyzed only incompletely. Negative Δg_{33} values arise partly from SOMO-virtual excitations. This agrees with the usual expectation that α−α couplings should contribute negatively to $\Delta g_{SO/OZ}$. However, except for $[(\mu\text{-adcO}^t\text{Bu})(CuL_2)_2]^{\bullet+}$, where $\beta-\beta$ couplings form doubly occupied MOs to SOMO contribute positively to all three tensor components, these couplings make an additional negative contribution to Δg_{33}. This suggests that the spin−orbit and orbital−Zeeman matrix elements may have the opposite sign (cf. eq 7), which usually strongly reflects off-center ring currents.[9] Obviously, the electronic situation in these ligand-centered complexes does not suit itself very well for a particularly simple interpretation of the **g**-tensor. However, we see clearly the stronger π-interactions between metal and bridging ligands for the azo compared with the tetrazine complexes, as reflected in the more positive Δg_{11} tensor components. The computationally somewhat more negative Δg_{33} for the tetrazine complexes mainly reflects a slightly larger role of SOMO-virtual excitations.

5. Conclusions

The study of these dinuclear copper complexes with bridging radical-anion ligands has provided us with more insight into the interrelations between electronic structure, spin density, and EPR parameters for this intriguing bonding situation than hitherto available. In particular, the ability of state-of-the art density functionals to describe metal and ligand hyperfine couplings and electronic **g**-tensors well (although no "best" functional is easily identified) allowed more detailed analyses than was possible for a previously studied test set of dinuclear rhenium complexes.[8]

The unexpected dependence of the isotropic metal hyperfine couplings on an exchange-correlation functional has drawn our attention to a subtle spin polarization of the σ-framework of the bridging ligand by the π-type SOMO. In analogy to the better-known McConnell mechanism in organic π-radicals, this spin polarization transfers some negative spin density into the copper 4s orbitals and thereby changes the origin of the negative isotropic metal hyperfine coupling fundamentally compared with the currently established picture of the mechanisms of transition-metal hyperfine couplings via core-shell spin polarization.[35]

Despite their clearly ligand-centered spin density, the title complexes exhibit appreciable electronic communication between the two metal centers. This is reflected in the EPR parameters, and it makes these types of "ligand-centered" radical complexes attractive as components of supermolecular functional materials.

Acknowledgment. We are grateful to W. Kaim and B. Sarkar (Stuttgart) for fruitful discussions. This work has been supported by Deutsche Forschungsgemeinschaft (Projects KA1187/4-2 and KA1187/7-1) and by the graduate college "Moderne Methoden der Magnetischen Resonanz" at Universität Stuttgart. C.R. thanks "Studienstiftung des Deutschen Volkes" for a scholarship.

Supporting Information Available: Table S1 with Cartesian coordinates of the optimized structures. Figure S1 showing the spin density distribution in the free ligand radical anions. This material is available free of charge via the Internet at http://pubs.acs.org.

References and Notes

(1) Stubbe, J.; van der Donk, W. A. *Chem. Rev.* **1998**, *98*, 705.

(2) See, for example, Kaim, W.; Schwederski, B. *Pure Appl. Chem.* **2004**, *76*, 351 and references therein.

(3) Chaudhuri, P.; Verani, C. N.; Bill, E.; Bothe, E.; Weyhermueller, T.; Wieghardt, K. *J. Am. Chem. Soc.* **2001**, *123*, 2213−2223.

(4) See, for example, Abragam, A.; Pryce, M. H. L. *Proc. R. Soc. London, Ser. A* **1951**, *205*, 135.

(5) Stone, A. J. *Mol. Phys.* **1963**, *6*, 509−515.

(6) Stone, A. J. *Mol. Phys.* **1964**, *7*, 311−316.

(7) Kaupp, M.; Bühl, M.; Malkin, V. G. *Calculation of NMR and EPR Parameters: Theory and Applications*; Wiley-VCH: Weinheim, Germany, 2004.

(8) Frantz, S.; Hartmann, H.; Doslik, N.; Wanner, M.; Kaim, W.; Kümmerer, H.-J.; Denninger, G.; Barra, A.-L.; Duboc-Toia, C.; Fiedler, J.; Ciofini, I.; Urban, C.; Kaupp, M. *J. Am. Chem. Soc.* **2002**, *124*, 10563−10571.

(9) Remenyi, C.; Kaupp, M. *J. Am. Chem. Soc.* **2005**, *127*, 11399−11413.
(10) Barra, A.-L.; Brunel, L.-C.; Baumann, F.; Schwach, M.; Moscherosch, M.; Kaim, W. *J. Chem. Soc., Dalton Trans.* **1999**, 3855−3857.
(11) Glöckle, M.; Huebler, K.; Kuemmerer, H.-J.; Denninger, G.; Kaim, W. *Inorg. Chem.* **2001**, *40*, 2263−2269.
(12) Kaim, W. *Coord. Chem. Rev.* **2002**, *230*, 127−139.
(13) Kaim, W.; Doslik, N.; Frantz, S.; Sixt, T.; Wanner, M.; Baumann, F.; Denninger, G.; Kummerer, H.-J.; Duboc-Toia, C.; Fiedler, J.; Zalis, S. *J. Mol. Struct.* **2003**, *656*, 183−194.
(14) Sarkar, B.; Frantz, S.; Kaim, W.; Duboc, C. *Dalton Trans.* **2004**, 3727−3731.
(15) Harriman, J. E. *Theoretical Foundations of Electron Spin Resonance*; Academic Press: New York, 1978.
(16) Abragam, A.; Bleaney, B. *Electron Paramagnetic Resonance of Transition Ions*; Clarendon Press: Oxford, U.K., 1970.
(17) Atherton, N. M. *Principles of Electron Spin Resonance*; Prentice Hall: New York, 1993.
(18) Weil, J. A.; Bolton, J. R.; Wertz, J. E. *Electron Paramagnetic Resonance: Elementary Theory and Practical Applications*; Wiley & Sons: New York, 1994.
(19) McGarvey, B. R. In *Transition Metal Chemistry: A Series of Advances*; Carlin, R. L., Ed.; Marcel Dekker, Inc.: New York, 1966; Vol. 3, pp 89−201.
(20) Mabbs, F. E.; Collison, D. *Electron Paramagnetic Resonance of d Transition Metal Compounds*; Elsevier: Amsterdam, The Netherlands, 1992.
(21) Neese, F. *J. Chem. Phys.* **2003**, *118*, 3939−3948.
(22) van Lenthe, E.; van der Avoird, A.; Wormer, P. E. S. *J. Chem. Phys.* **1998**, *108*, 4783−4796.
(23) Arbuznikov, A.; Vaara, J.; Kaupp, M. *J. Chem. Phys.* **2004**, *120*, 2127−2139.
(24) Remenyi, C.; Reviakine, R.; Arbuznikov, A. V.; Vaara, J.; Kaupp, M. *J. Phys. Chem. A* **2004**, *108*, 5026−5033.
(25) Malkina, O. L.; Vaara, J.; Schimmelpfennig, B.; Munzarová, M.; Malkin, V. G.; Kaupp, M. *J. Am. Chem. Soc.* **2000**, *122*, 9206−9218.
(26) Kaupp, M.; Reviakine, R.; Malkina, O. L.; Arbuznikov, A.; Schimmelpfennig, B.; Malkin, V. G. *J. Comput. Chem.* **2002**, *23*, 794−803.
(27) Schreckenbach, G.; Ziegler, T. *J. Phys. Chem. A* **1997**, *101*, 3388−3399.
(28) Neese, F. *J. Chem. Phys.* **2001**, *115*, 11080−11096.
(29) Becke, A. D. *Phys. Rev. A* **1988**, *38*, 3098.
(30) Perdew, J. P.; Wang, Y. *Phys. Rev. B* **1986**, *33*, 8822.
(31) Ahlrichs, R.; Bär, M.; Häser, M.; Horn, H.; Kölmel, C. *Chem. Phys. Lett.* **1989**, *162*, 165.
(32) Eichkorn, K.; Treutler, O.; Öhm, H.; Häser, M.; Ahlrich, R. *Chem. Phys. Lett.* **1995**, *240*, 283.
(33) Schäfer, A.; Horn, H.; Ahlrichs, R. *J. Chem. Phys.* **1992**, *97*, 2571−2577.
(34) Munzarová, M.; Kaupp, M. *J. Phys. Chem. A* **1999**, *103*, 9966−9983.
(35) Munzarová, M. L.; Kubácek, P.; Kaupp, M. *J. Am. Chem. Soc.* **2000**, *122*, 11900−11913.
(36) Kutzelnigg, W.; Fleischer, U.; Schindler, M. In *NMR Basic Principles and Progress*; Diehl, P., Fluck, E., Günther, H., Kosfeld, R., Seelig, J., Eds.; Springer-Verlag: Berlin, 1990; Vol. 23.
(37) Huzinaga, S. *Approximate Atomic Functions*; University of Alberta: Edmonton, Canada, 1971.
(38) Becke, A. D. *J. Chem. Phys.* **1993**, *98*, 5648.
(39) Stephens, P. J.; Devlin, F. J.; Chabalowski, C. F.; Frisch, M. J. *J. Phys. Chem.* **1994**, *98*, 11623−11627.
(40) Becke, A. D. *J. Chem. Phys.* **1993**, *98*, 1372.
(41) Lee, C.; Yang, W.; Parr, R. G. *Phys. Rev. B* **1988**, *37*, 785−789.
(42) Malkin, V. G.; Malkina, O. L.; Reviakine, R.; Arbouznikov, A. V.; Kaupp, M.; Schimmelpfennig, B.; Malkin, I.; Helgaker, T.; Ruud, K. *MAG-ReSpect*, version 1.2, 2004.
(43) Schimmelpfennig, B. *Atomic Spin−Orbit Mean-Field Integral Program*; Stockholms Universitet: Stockholm, Sweden, 1996.
(44) Hess, B. A.; Marian, C. M.; Wahlgren, U.; Gropen, O. *Chem. Phys. Lett.* **1996**, *251*, 365.
(45) Reed, A. E.; Weinstock, R. B.; Weinhold, F. *J. Chem. Phys.* **1985**, *83*, 735−746.
(46) Glendening, E. D.; Badenhoop, J. K.; Reed, A. E.; Carpenter, J. E.; Weinhold, F. *NBO4.M, version of NBO analysis programs*; Theoretical Chemistry Institute, University of Wisconsin: Madison, WI, 1999.
(47) Reviakine, R.; Kaupp, M. Unpublished results, Würzburg, Germany, 2004.
(48) Flükiger, P.; Lüthi, H. P.; Portmann, S.; Weber, J. *Molekel 4.0*; Swiss Center for Scientific Computing: Manno, Switzerland, 2000. See, for example, Portmann, S.; Lüthi, H. P. *Chimia* **2000**, *54*, 766.
(49) Schwach, M.; Hausen, H.-D.; Kaim, W. *Inorg. Chem.* **1999**, *38*, 2242−2243.
(50) Patchkovskii, S.; Ziegler, T. *J. Chem. Phys.* **1999**, *111*, 5730−5740.
(51) See, for example, Koch, W.; Holthausen, M. C. *A Chemist's Guide to Density Functional Theory*; Wiley-VCH: Weinheim, Germany, 2000.
(52) McConnell, H. M. *J. Chem. Phys.* **1956**, *24*, 764−766.
(53) Kaupp, M. In *EPR Spectroscopy of Free Radicals in Solids. Trends in Methods and Applications*; Lund, A., Shiotani, M., Eds.; Kluwer: Dordrecht, The Netherlands, 2002.
(54) Kaupp, M.; Asher, J.; Arbuznikov, A.; Patrakov, A. *Phys. Chem. Chem. Phys.* **2002**, *4*, 5458−5466.